



Cite this: DOI: 10.1039/d1sm00645b

Alignment of Au nanorods along *de novo* designed protein nanofibers studied with automated image analysis†

 Muammer Y. Yaman,^a Kathryn N. Guye,^a Maxim Ziatdinov,^b Hao Shen,^{cd} David Baker,^{cde} Sergei V. Kalinin^b and David S. Ginger^{*af}

In this study, we focus on exploring the directional assembly of anisotropic Au nanorods along *de novo* designed 1D protein nanofiber templates. Using machine learning and automated image processing, we analyze scanning electron microscopy (SEM) images to study how the attachment density and alignment fidelity are influenced by variables such as the aspect ratio of the Au nanorods, and the salt concentration of the solution. We find that the Au nanorods prefer to align parallel to the protein nanofibers. This preference decreases with increasing salt concentration, but is only weakly sensitive to the nanorod aspect ratio. While the overall specific Au nanorod attachment density to the protein fibers increases with increasing solution ionic strength, this increase is dominated primarily by non-specific binding to the substrate background, and we find that greater specific attachment (nanorods attached to the nanofiber template as compared to the substrates) occurs at the lower studied salt concentrations, with the maximum ratio of specific to non-specific binding occurring when the protein fiber solutions are prepared in 75 mM NaCl concentration.

 Received 30th April 2021,
 Accepted 8th June 2021

DOI: 10.1039/d1sm00645b

rsc.li/soft-matter-journal

Introduction

Hierarchically-organized hybrid organic/inorganic structures are interesting candidates for developing new advanced materials. Using programmable macromolecular building blocks such as proteins,^{1–3} peptoids,^{4–7} and polymers^{8–16} as templating agents to scaffold the assembly of functional inorganic building blocks is one approach to achieve this goal. It can be advantageous, for example, to combine the programmable atomic-precision afforded by biomolecular self-assembly, with the optical and electronic properties of inorganic materials. These materials are important in fields ranging from plasmonics,^{11,17,18} to quantum optics,^{19,20} and biosensing.^{21–23} Kotov and co-workers recently used protein²⁴ and peptide²⁵ templates to direct the assembly of

gold nanorods to produce chiroptical structures with record chiral dichroism and optical asymmetry *g*-factors.²⁵

In pursuing such approaches, a key challenge is to understand and control the physical interactions between the inorganic building blocks and the biological templates, especially at the interfaces. Understanding these processes can provide guide rules for future design and rational synthesis of hierarchical materials. Electrostatic interactions are classic and widely used, yet still an interesting area to explore. For example, by controlling salt concentration, which affects the electrostatic force at the protein–mineral interfaces, Pyles *et al.* showed the orientation proteins prefer to attach to an inorganic substrate can be tailored by varying the ionic strength of the solution.²⁶

Here, we explore the converse problem: what factors control the fidelity of alignment of metal nanorods with protein fibers acting as the assembly templates. We use a *de novo* designed protein fiber²⁷ engineered to have a very high density of negatively-charged surface residues, under neutral conditions, as a template to drive the electrostatic assembly of positively-charged gold nanorods along the nanofiber axis. We conduct a series of experiments varying the external parameters such as the aspect ratio of the Au nanorods and the salt concentration (ionic strength) to assess how they affect the assembly of the Au nanorods on the protein fibers relative to an aminosilanized ITO substrate. We develop and apply an automated image analysis tool to facilitate analysis of the experimental data.

^a Department of Chemistry, University of Washington, Seattle, WA, USA.

 E-mail: dginger@uw.edu
^b Center for Nanophase Materials Sciences, Oak Ridge National Laboratory, Oak Ridge, TN, USA

^c Department of Biochemistry, University of Washington, Seattle, WA, USA

^d Institute for Protein Design, University of Washington, Seattle, WA, USA

^e Howard Hughes Medical Institute, University of Washington, Seattle, WA, USA

^f Physical Sciences Division, Physical and Computational Sciences Directorate, Pacific Northwest National Laboratory, Richland, WA, USA

† Electronic supplementary information (ESI) available. See DOI: 10.1039/d1sm00645b

We find that the fidelity of the electrostatically-driven self-assembly of Au nanorods onto protein nanofiber templates depends on the aspect ratio of the nanorods, as well as the ionic strength of the solution.

Result and discussion

Fig. 1(a) shows a schematic of our assembly approach for attaching Au nanorods onto pre-assembled *de novo* designed protein nanofibers (see ESI† for full details). Briefly, we drop cast pre-assembled protein fibers²⁷ onto positively-charged silane-coated ITO substrates. As a monolayer on ITO substrate, the silane, (3-aminopropyl)triethoxysilane, has a pK_a of 7.6.^{28,29} Thus, when the protein is deposited in a pH 8 tris buffer, the silane surface remains partially protonated, yielding a net positive charge, to which the negatively-charged proteins can attach due to a combination of electrostatic and van der Waals attraction.^{29,30} Next, as shown, we exposed these positively-charged surfaces to solutions of preassembled protein nanofibers. We designed the protein nanofibers to have a high-density of carboxylic acid groups on their surfaces,²⁷ decorating them with a net negative surface charge in buffer at pH 8. Due to the electrostatic attraction, the negatively-charged protein fibers attach at high densities to the charged silane (see the SEM image in Fig. 1a). The protein nanofibers attach at much lower density (if at all) to substrates without silane treatment (see Fig. S1, ESI†).

Next, following attachment of the protein nanofibers, we exposed the substrates to solutions of Au nanorods synthesized by the method of Ye *et al.*³¹ Terminated with cetyl trimethyl ammonium (CTA) cations, these Au nanorods have a net positive charge,³² and thus are candidates for electrostatically-driven self-assembly onto the protein nanofibers. Due to the large density of the Au nanorods, we performed the nanorod attachment step with inverted substrates (Fig. 1) in order to allow the assembly process be dominated by short-range interactions while eliminating the potential for gravitational sedimentation.

We then gently washed the substrates with distilled water to remove the excess Au nanorod solution, and imaged the resulting structures using scanning electron microscopy (SEM). Fig. 1(b) shows the resulting Au nanorod decorated protein nanofibers. In these images the nanofibers appear clearly as black lines stretching for several microns, while the Au nanorods appear as bright white cylindrically-shaped objects. We used the ITO substrate to perform SEM imaging on a conductive surface without the need to sputter over the structures. However, the grain structure of the ITO is also faintly visible in the background. While the ITO grain boundaries also appear as black lines, they are much lighter and thinner than the protein nanofibers, and are easily distinguished from the protein.

We observed that protein nanofibers attached on functionalized ITO at a reasonably high density ($2.5 \pm 1.3 \mu\text{m}$ protein nanofibers per μm^2 area) (see Fig. S2A, ESI†) for solutions with different concentrations of salt between 25 mM and 1 M, and the average density of protein fibers for each solution are quite similar. On the contrary, the Au nanorods were attached primarily to the nanofibers or to the substrate with different densities in 25 ± 13 particles per μm^2 area, which depend on the sample and attachment conditions (see Fig. S2B, ESI†).

In order to explore how different variables affect the fidelity of the assembly of Au nanorods along the protein nanofibers, we performed a number of experiments as a function of nanorod aspect ratio, and ionic strength of the solution. In order to efficiently generate statistically-robust data sets and to automate the workflow for future experiments, we utilized a python-based automatic image analysis tool.^{33,34} In this context, the goal for such an image analysis tool is to automatically recognize the protein fibers and label Au nanorods as attached to protein fibers or substrate under different experimental conditions. Here we consider binding to the protein fibers as specific binding, and to the substrate as non-specific binding. In addition, the image analysis tool should provide additional information concerning the angle of each Au nanorod on protein fibers, the size distribution of nanorods, and the length of protein fibers. All this information together should help to

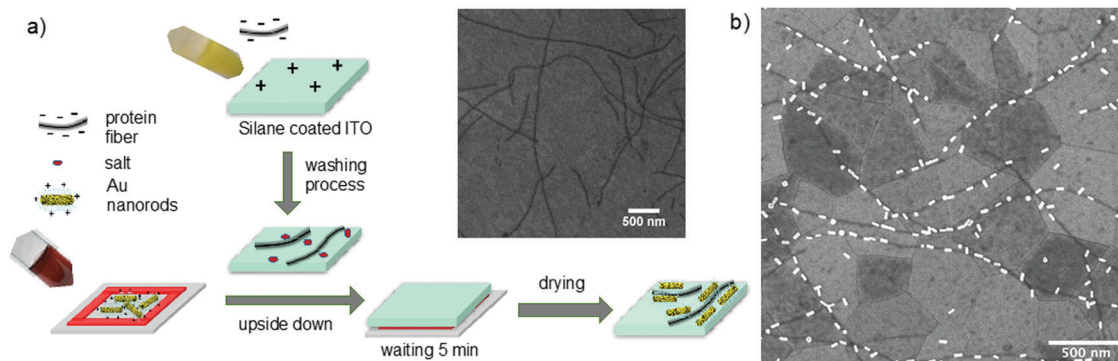


Fig. 1 (a) Schematic representation of the assembly process and a SEM image of protein fibers on a silane-treated ITO substrate. The protein fibers were drop cast onto the silane-coated ITO substrate and then the substrate was put upside-down on the top of the chamber filled with Au nanorods in solution (to avoid attachment by sedimentation). The substrate was gently washed and dried for imaging. (b) An SEM image of Au-decorated *de novo* designed protein nanofibers.

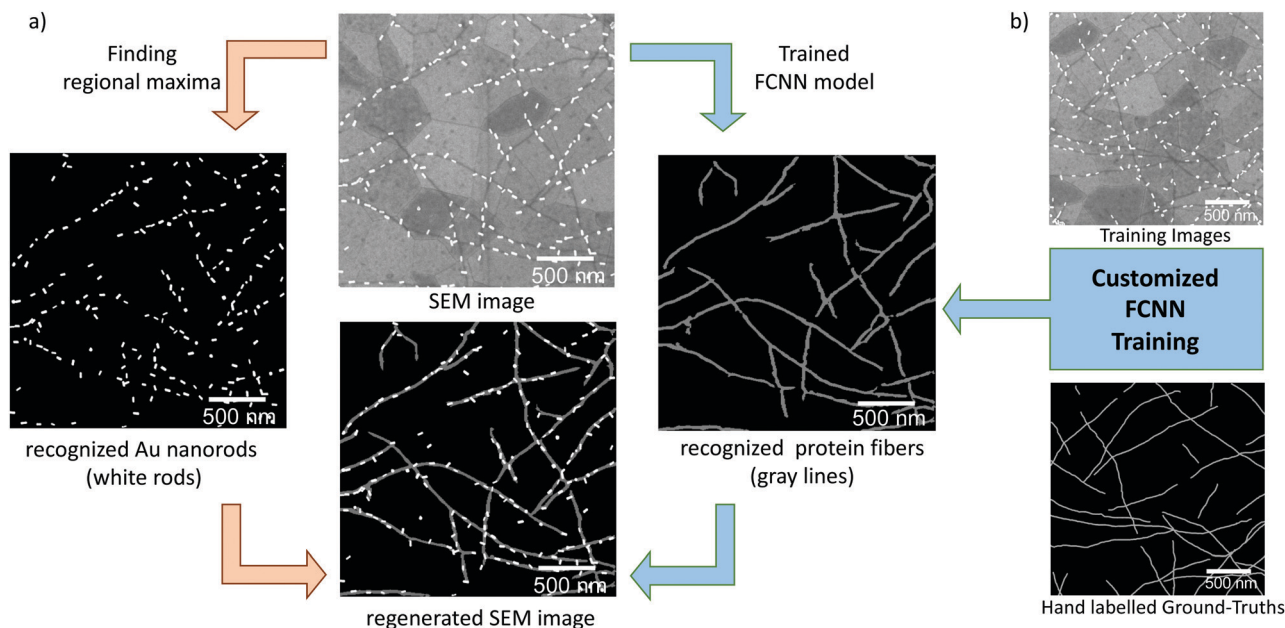


Fig. 2 (a) Schematic representation of our automated SEM image analysis tool. (b) Training process of the Fully Convolutional Neural Network (FCNN) model for recognizing the protein fibers.

analyze each individual particle and hopefully will contribute to our understanding of local surface–surface interactions at the nanoscale.

Fig. 2 shows the workflow of the automated image analysis tool. Firstly, the contrast of the images was adjusted and then filtered regional maxima to find bright gold particles in the image. Next, we utilized a fully convolutional neural network (FCNN) to separate the protein fibers from the rest of the image.^{34,35} Specifically, the FCNN performed a semantic segmentation of the input images by categorizing every pixel in the image as belonging to a fiber or to a background.³⁶ The FCNN structure is based on the custom-build dilnet architecture,³⁷ which uses only a single max-pooling (and the corresponding up-sampling) operation to preserve the maximum amount of information and utilizes dilated convolutions to reduce the total number of weights to train. The latter reduces a computational cost and allows training the FCNN for the large-size images. To train the FCNN, we created image-mask pairs by hand labelling a small subset of experimental images and performing the standard data augmentation procedure, which included random cropping, rotation, and horizontal/vertical flipping. The FCNN weights were optimized using the Adam extension³⁸ of the stochastic gradient descent algorithm using with the binary cross-entropy loss objective. Once the loss reaches a plateau (with the value of ~ 0.1), the predicted morphology of protein fibers is adopted for further analysis. Finally, the new image was automatically regenerated from both outputs.

After assigning the position of the nanofibers using the FCNN, and the positions of the bright white Au nanorods using thresholding, we then analyzed the resulting labeled images. We used custom automated image analysis tools to compute

properties, such as Au nanorod particle size and aspect ratio, and to quantify specific Au nanorods attachment on protein fibers, and non-specific Au nanorods attachment to the substrate. We also used these tools to compute the angle that the axis of each specifically attached Au nanorod made with respect to the tangent to the local protein nanofiber axis.

After developing the automatic image analysis tool, we first investigated the effect of solution ionic strength on the attachment of the Au nanorods to the protein fibers. We used 25 mM, 75 mM, 150 mM, and 1 M NaCl solutions. We note that these NaCl concentrations were those applied to the protein buffer conditions during assembly, and that the salt concentrations were lower at the final stages of assembly because of the washing steps – but we anticipate that by the washing step the assembly was mostly completed (as verified by the significant differences in particle assembly results based on ionic strength). Fig. 3(a) shows the resulting morphologies of the final assembled nanofiber/nanorod solutions. Those images were generated using the image analysis tool, with the protein nanofibers labelled with a gray line, and the Au nanorods labelled with a white rod shape. Fig. S2 (ESI[†]) shows the corresponding raw SEM images.

Fig. 3(b) shows the number of Au nanorods specifically bound to protein fibers at varying salt concentrations. We quantified the results from the regenerated images as done by the automated image analysis tool. To get statistically-robust results, we analyzed multiple regions on the substrates ensuring that the total number of analyzed particles is more than 500 particles for each sample. The *x*-axis shows the NaCl concentration while the *y*-axis (the green bins) shows the number of Au nanorods specifically attached per 1 μm protein fibers. The average length and width for the Au nanorods from

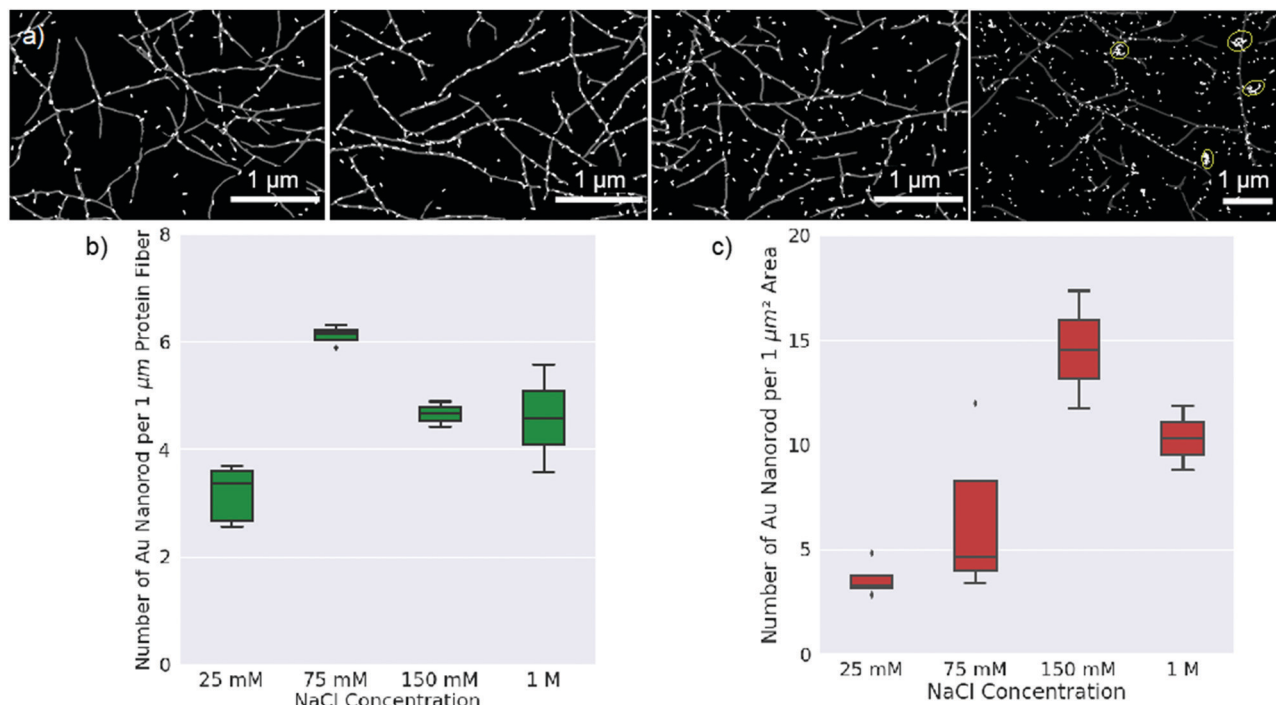


Fig. 3 (a) Processed and labelled SEM images at different NaCl concentration from 25 mM to 1 M (from left to right). The gray lines show protein fibers and the white particles show the Au nanorods. The aggregated Au NRs were labelled with yellow lines. (b) Boxplots show the results from the images analyzed with our automated image analysis tool. The x-axis shows the NaCl concentration whereas the y-axis (the green bins) shows the number of specific Au nanorod attachment per 1 μm protein fibers (c) Boxplot of results the above images from the automated image analysis tools. The y-axis (the red bins) shows the number of non-specific Au nanorod attachments per the 1 μm² substrate.

this solution are 45 ± 9 nm and 19 ± 5 nm, respectively. Thus, the maximum loading density of 45 nm-long Au nanorods is 22 nanorods ($22 = 1 \mu\text{m}/45 \text{ nm}$) per micron of nanofiber if the Au nanorods were to stack perfectly head-to-tail along the protein fibers. We constrained the density to one particle per section of the protein fiber, because the protein fiber and Au nanorods have similar diameters (~ 15 nm), however in other work with larger fibers it is possible to assemble multiple nanorods on fibers of sufficient width.¹⁶ The highest specific Au attachment to protein fibers was observed when the protein fiber solution is prepared in 75 mM NaCl concentration. As the salt concentration increases, the number of specifically attached Au nanorods first increases at moderate concentration (75 mM NaCl) to maximize the specific electrostatic attraction and then decreases at higher concentration (150 mM and 1 M NaCl) within the limits of experimental uncertainty, we propose this trend can be explained by a balancing of competing factors. When the ionic strength is too low the nanorods can repel each other, and also see repulsion from the background substrate, reducing the attachment density. At intermediate salt concentrations, the rods are screened from all but the shortest-range interactions and can achieve a higher density of attachment to the fibers, while above 75 mM, all electrostatic forces are screened too greatly, resulting in poor particle–substrate repulsion and poor particle–fiber attraction, and leading to non-specific van der Waals attraction as the driving force of assembly. Here, we see that the maximum value reaches

6 particles per micron of fiber for the 75 mM NaCl solution, indicating that the nanorods are occupying just under 1/3 of the available protein surface.

Fig. 3c shows the quantitative results for non-specific attachment of Au nanorods (NRs) to the silane-treated ITO substrate. In this case, the y-axis shows the number of attached Au particles per area (1 μm²) and the area for each image is 9 μm². The number of non-specifically attached Au nanorods (shown in red bins) increases as the salt concentration increases. However, the number of attached Au nanorods decreases at the highest salt concentration (1 M NaCl), most likely because at such high salt concentrations, the Au nanorods quickly aggregate and settle down to the bottom of the reaction chamber due to the gravitational force. We did not observe any aggregated Au nanorods on the substrate except when the protein fiber solution is prepared in 1 M NaCl. The aggregated Au nanorods were labelled with yellow lines in Fig. 3a.

We also prepared different Au nanorod solutions with different aspect ratios ranging from 2 to 5, (see ESI,† Materials and methods section and Table S2) to examine the effect of the aspect ratio of Au on the attachment process. While we hypothesized that the aspect ratio of the nanorod might play a role, we observe similar behavior in all cases over the size range that was readily accessible experimentally (see Fig. S3 and S4, ESI†).

Finally, after analyzing the attachment density of the Au nanorods, we further explored how the attachment angle of the

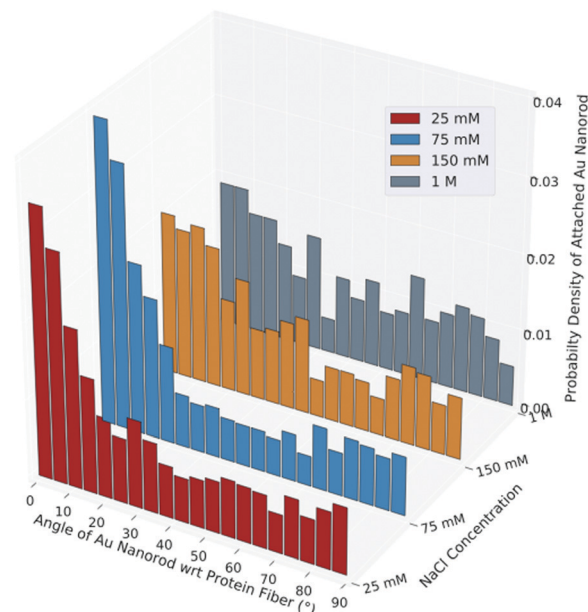


Fig. 4 Plot of angular distribution of Au nanorods attached to the protein fiber. The x-axis shows the angle of Au nanorods with respect to the protein fiber, the y-axis shows the different salt concentrations and the z-axis shows the probability density of attached Au NRs. The 25 mM and 75 mM salt concentrations both show peaks at narrow angles < 20 degrees, while at higher salt concentration the attachment becomes more random.

nanorods with respect to the protein fibers axis and the inter-rod distance changed with the solution salt concentration. The automated image analysis tool creates a sub image for each individual gold particle and then finds the best fit line for the orientation of the protein fibers in the sub image using the Hough Line Transform.³⁹ It then calculates the angle at the intersection between Au nanorod and protein fiber for each particle. Fig. 4 shows the resulting normalized angular distributions of the attached Au nanorod to the protein fibers. We clearly see that at 25 mM and 75 mM salt concentration, the Au nanorods are preferentially aligned with the nanofibers (with nearly 60% of the nanorods aligned with less than a 20° angle with respect to the particle axis). However, when we increase the salt concentration, both mean and median angles of the distribution increase and the spread in attachment angles of the Au nanorods also increases, indicating that attachment becomes more random and less specific at higher salt concentration. By the time we reach 1 M salt concentration, the probability of the attachment angle of the Au nanorod to the protein fiber is almost equal and there is no favorable attachment angle.

We calculate pair distribution functions (PDFs) for the Au nanorods as a function of ionic strength in Fig. S7 (ESI[†]). Notably, the PDF at lower salt concentrations has a peak at smaller distances, which we interpret as reflecting the preferential assembly along the nanofibers at low ionic strength leading to more closely spaced rods. At higher salt concentration the random distribution of rods across the entire surface leads to a shift to larger distances, while at very high (1 M) salt the extremely high density of random attachment leads to a shift back to smaller values.

Both results from Fig. 4 and Fig. S7 (ESI[†]) are consistent with our observations of a transition from specific electrostatic attachment to the protein fibers at low salt (25 mM and 75 mM) to non-specific binding to the substrate at higher salt (150 mM and 1 M). At low salt concentrations, the Au nanorods tend to maximize the favorable electrostatic attraction between the length of the rod and the length of the fiber by aligning the same direction, whereas at higher salt concentrations, they are randomly aligned and really have little preference for the protein fiber over the substrate. It is possible that at lower salt concentrations the particles are able to move more freely to find the orientation of lowest potential energy whereas at high ionic strength, with the Coulomb repulsion terms that prevent nanorod attachment to the glass substrate screened, nanorods tend to stick where they first attach, with more random orientations.

Conclusions

In summary, we show that *de novo* designed proteins with high surface charge densities can be used successfully to assemble, and align, Au nanorods. We further show that the salt concentration can be tuned to achieve ordered and disordered assemblies. The optimum salt concentration of 75 mM for these nanofibers likely achieves as balance between particle–particle and particle–substrate interactions, without resulting in significant particle aggregation and non-specific binding. Importantly, we developed, and have made publicly available,⁴⁰ image analysis tools utilizing a fully convolutional neural network to analyze experimental data and gain geometrical information

from each nanorod and nanofiber. This work is an important step towards reliable self-assembly of functional inorganic building blocks along these designer protein templates. Future studies may explore alternative *de novo* designed proteins combining both electrostatic and covalent interactions, as well as seek to explore the emergent optoelectronic properties of these systems. Developing optical screening methods that allow particle assembly to be analyzed in real time and *in situ* during assembly, without requiring *ex situ* electron microscopy analysis would also be valuable.

Author contributions

The project was planned by M. Y. Y., K. G., S. H., D. B. and D. S. G. The Au nanorods and protein fibers were synthesized by M. Y. Y. and S. H., respectively. The automated image analysis tool developed M. Y. Y., M. Z. and S. V. K. and scanning electron microscopy were done by M. Y. Y. The paper was written by M. Y. Y., K. G. and D. S. G. with input from all authors. D. B. and D. S. G. supervised the project.

Conflicts of interest

There are no conflicts to declare.

Acknowledgements

This material is based upon work supported by the US Department of Energy, Office of Science, Office of Basic Energy Sciences, as part of the Energy Frontier Research Centers program: CSSAS-The Center for the Science of Synthesis Across Scales under Award Number DE-SC0019288. SEM imaging was conducted at the University of Washington Molecular Analysis Facility, a National Nanotechnology Coordinated Infrastructure (NNCI) site which is supported in part by the National Science Foundation, (Grant NNCI-1542101), the University of Washington, the Molecular Engineering and Sciences Institute, and the Clean Energy Institute. M. Y. acknowledges support from the University of Washington Clean Energy Institute and the National Science Foundation Research Traineeship under Award NSF DGE-1633216. D. S. G. acknowledges support from the University of Washington, Department of Chemistry Kwiram Endowment.

Notes and references

- J. Dou, A. A. Vorobieva, W. Sheffler, L. A. Doyle, H. Park, M. J. Bick, B. Mao, G. W. Foight, M. Y. Lee, L. A. Gagnon, L. Carter, B. Sankaran, S. Ovchinnikov, E. Marcos, P. S. Huang, J. C. Vaughan, B. L. Stoddard and D. Baker, *Nature*, 2018, **561**, 485–491.
- P. Fratzl and R. Weinkamer, *Prog. Mater. Sci.*, 2007, **52**, 1263–1334.
- G. Nyström, L. Roder, M. P. Fernández-Ronco and R. Mezzenga, *Adv. Funct. Mater.*, 2018, **28**, 1703609.
- F. Yan, L. Liu, T. R. Walsh, Y. Gong, P. Z. El-Khoury, Y. Zhang, Z. Zhu, J. J. De Yoreo, M. H. Engelhard, X. Zhang and C.-L. Chen, *Nat. Commun.*, 2018, **9**, 2327.
- J. Ma, B. Cai, S. Zhang, T. Jian, J. J. De Yoreo, C.-L. Chen and F. Baneyx, *Nano Lett.*, 2021, **21**, 1636–1642.
- M. Monahan, B. Cai, T. Jian, S. Zhang, G. Zhu, C.-L. Chen, J. J. De Yoreo and B. M. Cossairt, *Nanoscale*, 2021, **13**, 1273–1282.
- C.-L. Chen, P. Zhang and N. L. Rosi, *J. Am. Chem. Soc.*, 2008, **130**, 13555–13557.
- Y. Yu, Y. He, Z. Mu, Y. Zhao, K. Kong, Z. Liu and R. Tang, *Adv. Funct. Mater.*, 2020, **30**, 1908556.
- M. Kijima, Y. Oaki, Y. Munekawa and H. Imai, *Chem. – Eur. J.*, 2013, **19**, 2284–2293.
- N. Bridonneau, V. Noël, S. Zrig and F. Carn, *J. Phys. Chem. B*, 2020, **124**, 900–908.
- V. Myroshnychenko, J. Rodriguez-Fernandez, I. Pastoriza-Santos, A. M. Funston, C. Novo, P. Mulvaney, L. M. Liz-Marzan and F. J. G. de Abajo, *Chem. Soc. Rev.*, 2008, **37**, 1792.
- P. Bai, S. Yang, W. Bao, J. Kao, K. Thorkelsson, M. Salmeron, X. Zhang and T. Xu, *Nano Lett.*, 2017, **17**, 6847–6854.
- Z. Liu, H. Huang and T. He, *Small*, 2013, **9**, 505–510.
- C. Yi, H. Liu, S. Zhang, Y. Yang, Y. Zhang, Z. Lu, E. Kumacheva and Z. Nie, *Science*, 2020, **369**, 1369–1374.
- K. Liu, Z. Nie, N. Zhao, W. Li, M. Rubinstein and E. Kumacheva, *Science*, 2010, **329**, 197–200.
- C. H. Lee, L. Tian, A. Abbas, R. Kattumenu and S. Singamaneni, *Nanotechnology*, 2011, **22**, 275311.
- A. D. Merg, J. C. Boatz, A. Mandal, G. Zhao, S. Mokashi-Punekar, C. Liu, X. Wang, P. Zhang, P. C. A. van der Wel and N. L. Rosi, *J. Am. Chem. Soc.*, 2016, **138**, 13655–13663.
- F. Neubrech, M. Hentschel and N. Liu, *Adv. Mater.*, 2020, **32**, 1905640.
- Z. Qian and D. S. Ginger, *J. Am. Chem. Soc.*, 2017, **139**, 5266–5276.
- V. Amendola, R. Pilot, M. Frasconi, O. M. Maragò and M. A. Iati, *J. Phys.: Condens. Matter*, 2017, **29**, 203002.
- P. Hao, Y. Wu and F. Li, *Appl. Opt.*, 2011, **50**, 5555.
- A. V. Kabashin, P. Evans, S. Pastkovsky, W. Hendren, G. A. Wurtz, R. Atkinson, R. Pollard, V. A. Podolskiy and A. V. Zayats, *Nat. Mater.*, 2009, **8**, 867.
- X. Xue, F. Wang and X. Liu, *J. Mater. Chem.*, 2011, **21**, 13107.
- W. Jiang, Z. Qu, P. Kumar, D. Vecchio, Y. Wang, Y. Ma, J. H. Bahng, K. Bernardino, W. R. Gomes, F. M. Colombari, A. Lozada-Blanco, M. Veksler, E. Marino, A. Simon, C. Murray, S. R. Muniz, A. F. de Moura and N. A. Kotov, *Science*, 2020, eaaz7949.
- J. Lu, Y. Xue, K. Bernardino, N.-N. Zhang, W. R. Gomes, N. S. Ramesar, S. Liu, Z. Hu, T. Sun, A. F. de Moura, N. A. Kotov and K. Liu, *Science*, 2021, **371**, 1368–1374.
- H. Pyles, S. Zhang, J. J. De Yoreo and D. Baker, *Nature*, 2019, **571**, 251–256.
- H. Shen, J. A. Fallas, E. Lynch, W. Sheffler, B. Parry, N. Jannetty, J. Decarreau, M. Wagenbach, J. J. Vicente,

- J. Chen, L. Wang, Q. Dowling, G. Oberdorfer, L. Stewart, L. Wordeman, J. De Yoreo, C. Jacobs-Wagner, J. Kollman and D. Baker, *Science*, 2018, **362**, 705.
- 28 N. Fang, H. Lee, C. Sun and X. Zhang, *Science*, 2005, **308**, 534.
- 29 R. R. Bhat and J. Genzer, *Nanotechnology*, 2007, **18**, 025301.
- 30 M. Valtiner, X. Banquy, K. Kristiansen, G. W. Greene and J. N. Israelachvili, *Langmuir*, 2012, **28**, 13080–13093.
- 31 X. Ye, L. Jin, H. Caglayan, J. Chen, G. Xing, C. Zheng, V. Doan-Nguyen, Y. Kang, N. Engheta, C. R. Kagan and C. B. Murray, *ACS Nano*, 2012, **6**, 2804–2817.
- 32 J.-Y. Kim, M.-G. Han, M.-B. Lien, S. Magonov, Y. Zhu, H. George, T. B. Norris and N. A. Kotov, *Sci. Adv.*, 2018, **4**, e1700682.
- 33 M. Ziatdinov, O. Dyck, A. Maksov, X. Li, X. Sang, K. Xiao, R. R. Unocic, R. Vasudevan, S. Jesse and S. V. Kalinin, *ACS Nano*, 2017, **11**, 12742–12752.
- 34 M. Ziatdinov, S. Zhang, O. Dollar, J. Pfaendtner, C. J. Mundy, X. Li, H. Pyles, D. Baker, J. J. De Yoreo and S. V. Kalinin, *Nano Lett.*, 2020, **21**, 158–165.
- 35 S. V. Kalinin, S. Zhang, M. Valletti, H. Pyles, D. Baker, J. J. De Yoreo and M. Ziatdinov, *ACS Nano*, 2021, **15**, 6471–6480.
- 36 F. Chollet, *Deep learning with Python*, 2018.
- 37 M. Ziatdinov, AtomAI, GitHub repository, <https://github.com/pycrosopy/atomai>.
- 38 D. P. Kingma and J. Ba, 2013, arXiv:1312.6114.
- 39 R. O. Duda and P. E. Hart, *Commun. ACM*, 1972, **15**, 11–15.
- 40 M. Yaman, GitHub repository, https://github.com/yamanmy/Automated_image_tool_for_Au_PF_image.